Effect of surface tension on the acoustic radiation pressure–induced motion of the water–air interface

C. Cinbis
Edward L. Ginzton Laboratory, Stanford University, Stanford, California 94305-4085

N. N. Mansour
General Science and Technology, 491 Macara Ave., Suite 1007, Sunnyvale, California 94086

B. T. Khuri-Yakub
Edward L. Ginzton Laboratory, Stanford University, Stanford, California 94305-4085

(Received 30 September 1992; accepted for publication 8 June 1993)

The displacement of a water–air interface and its relaxation as a function of acoustic energy density and surface tension were analyzed both experimentally and numerically. Experimental systems were devised to observe the time evolution of the surface. A theoretical model to predict the response of the interface to acoustic excitation was also developed. It was found that the Langevin pressure due to a focused acoustic beam will cause the interface to rise to a height that is a function of the energy density of the beam. The rise time, which is the time it takes for the wafer surface to rise to its maximum height, was found to be independent of the incident energy, but was found to be a function of the surface tension. The time of mound formation measurements in clean water at low-energy acoustic excitations were found to be within 20% of the simulation results. These results imply that surface rise time measurements may present a novel way of measuring surface tension of water–surfactant combinations accurately and rapidly by a simple noncontacting technique.

PACS numbers: 43.25.Qp

INTRODUCTION

Interaction of acoustic waves with liquid interfaces via acoustic radiation pressure has been the subject of many interesting articles. The basic concept of acoustic radiation pressure was first studied by Lord Rayleigh[1,2] in 1902. The differences between the two types of radiation pressure, called Rayleigh and Langevin radiation pressure, were discussed and clarified by the works of Beyer,[3] Rooney and Nyborg,[4] and Chu and Apfel.[5] Many physical phenomena and applications,[6] such as acoustic streaming, radiation force measurements, acoustic levitation, ultrasonic atomization, and droplet formation, are examples of new fields of research that emerged following the developments in this area. Among them, droplet formation via focused acoustic beams, as discussed by Elrod *et al.*,[7] is particularly related to our work. In their case, they investigated the dynamics of nozzleless droplet formation, such as droplet formation time and drop size, as a function of ultrasound frequency and pulse width. In the present work we use a focused acoustic beam at a wafer–air interface to form a mound on the interface. We measure the height of the mound and the time it takes for the wafer surface to rise to its maximum height. Our objective is to investigate the effects of surface tension on mound formation.

We use a boundary integral method to analyze the surface deformation caused by a focused acoustic beam at a water–air interface. In this analysis, we mainly concentrate on the effects of the surface tension and the incident acoustic energy on the surface displacement and the surface rise time. Our results show that the rise time is weakly dependent on the incident acoustic pulse energy, provided that the energy is kept below a certain threshold. We find that the rise time is a strong function of surface tension.

The experimental technique for measuring the above parameters is shown in Fig. 1. We alter the surface tension of water by adding small amounts of surfactants, and measure their effect on the time of mound formation. For this purpose, we use 3-MHz focused ultrasonic transducers with f numbers of 1 and 3. The transducers are excited with an electrical tone burst. The liquid surface is adjusted to be at the focal plane of the transducer by monitoring the time of flight of the acoustic echoes from the surface. By the application of a burst of acoustic energy, a mound rises up from the water surface and relaxes back to its equilibrium position. The mound is also the source of transient capillary waves propagating radially outward from the acoustical focus. Their characteristics can be analyzed by a phase inversion technique for measuring surface tension.[8] This technique is not discussed in this paper. A confocal optical microscope positioned above the water surface senses the displacement of the interface at the center of the mound.[8]

I. RADIATION PRESSURE

In order to calculate the incident pressure profile from the acoustic transducer at its focal plane, we use the expression for Langevin radiation pressure P_L. It is defined as the time-averaged pressure experienced by a plane target placed in the path of an unconfined acoustic beam. At an

 0001-4966/93/94(4)/2365/8/$6.00 © 1993 Acoustical Society of America

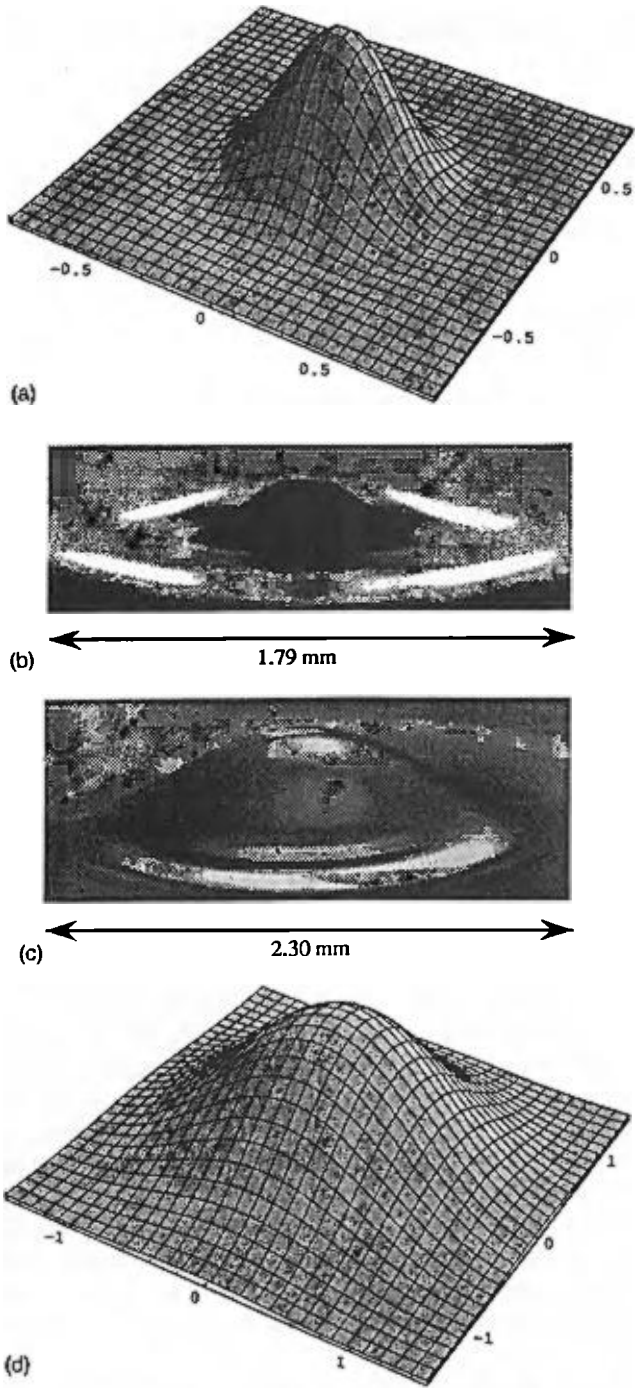

FIG. 1. Comparison of theoretically calculated acoustic radiation profiles with experimentally observed mound profiles, for (a) and (b) an $f-1$ transducer, and (c) and (d), an $f-3$ transducer operating at 3 MHz in water.

interface between a liquid and a pressure-release surface such as air, radiation pressure can be shown to be[7]

$$P_L=2I_i/c, \tag{1}$$

where I_i is the average intensity of the incident acoustic beam, and c is the speed of sound in the liquid. We are justified to use this expression, since the wave front is planar and parallel to the surface at the focal plane.

The field intensity at the focal plane of a focused transducer[9] can be written as

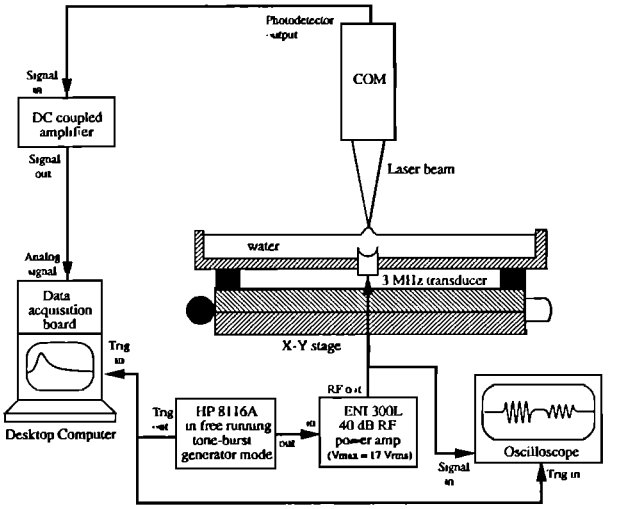

FIG. 2. Experimental arrangement for measuring the rise time of the water surface with acoustic excitation as a function of surface tension.

$$P_L(r)=2(I_0/c)\text{jinc}^2(ra/z_0\lambda), \tag{2}$$

where r is the radial distance away from the focus, I_0 is the peak intensity at $r=0$, a and z_0 are the radius and the focal length of the transducer, respectively, and λ is the wavelength of the acoustic wave in the medium. In order to evaluate the radiation pressure distribution at the surface, one has to know the total instantaneous power incident at the liquid–air interface. If η is the power conversion efficiency of the transducer, V_p is the peak voltage applied at the transducer terminals, and R is the electrical input impedance of the transducer, then we can write

$$P_L(r)=0.1012\pi\frac{\eta V_p^2}{cR}\left(\frac{a}{\lambda z_0}\right)^2\text{jinc}^2\left(\frac{ra}{z_0\lambda}\right). \tag{3}$$

This equation is used to determine the Langevin radiation pressure for the transducer geometries involved as we proceed to calculate the initial velocity potential for the mound formation analysis. In Fig. 2, we show theoretically calculated normalized radiation pressure profiles at the focal plane of a 3-MHz focused transducer with f numbers of 1 and 3. Also shown in Fig. 2 is a comparison of the theoretical profiles to stroboscopically imaged water surface displacement via the acoustic radiation pressure generated by focused transducers of the same parameters. As seen, experimentally observed profiles have general characteristics that match well with the pressure profile expressed in Eq. (3).

II. VELOCITY POTENTIAL ANALYSIS OF MOUND FORMATION

This theoretical formalism was originally developed to study the oscillations of drops in zero gravity. It was used to study the breakup of capillary jets into main and satellite drops.[10] The following is an adaptation of this theory to include the effect of gravity, which may not be negligible.

A. The initial potential

At the free surface, the unsteady Bernoulli's equation is

$$\frac{d\Phi}{dt}=-\frac{p}{\rho}+gz+\frac{1}{2}\mathbf{u}\cdot\mathbf{u}, \tag{4}$$

where Φ is the velocity potential, p is the pressure, ρ is the density, and $\mathbf{u}=\nabla\Phi$ is the velocity. If we integrate the above equation in time, we get

$$\Phi-\Phi_0=\int_0^{\Delta t}\frac{p}{\rho}dt+gz\,\Delta t+\frac{1}{2}\int_0^{\Delta t}\nabla\Phi(\tau)\cdot\nabla\Phi(\tau)d\tau. \tag{5}$$

For stationary initial conditions, we take $\Phi_0=0$. We assume that the radiation pressure is such that the first integral on the right-hand side of the above equation is finite. The last term is such that

$$\int_0^{\Delta t}\nabla\Phi(\tau)\cdot\nabla\Phi(\tau)d\tau<\nabla\Phi\cdot\nabla\Phi\Delta t, \tag{6}$$

since the kernel in the integral is positive and definite. For short times this integral and the term $gz\Delta t$ can be neglected. We then have

$$\Phi=(P_L/\rho)\Delta t, \tag{7}$$

where P_L is the Langevin radiation pressure, as given in Eq. (3).

Using scaling parameters, we can perform the analysis in dimensionless form. From the expression of radiation pressure in Eq. (3), we see that the relevant length scale is

$$L=\lambda z_0/a. \tag{8}$$

The f number of a lens is defined as

$$F=z_0/2a, \tag{9}$$

which yields

$$L=2\lambda F. \tag{10}$$

The surface tension σ, the density ρ, and the length scale L yield a velocity scale

$$V=\sqrt{2\sigma/\rho L} \tag{11}$$

and a time scale T as L over V, which becomes

$$T=2\lambda^{3/2}F^{3/2}\rho^{1/2}/\sigma^{1/2}. \tag{12}$$

Using the above scaling parameters, we can convert the velocity potential Φ given by Eq. (7) into a dimensionless form ϕ by using Eqs. (9)–(11) such that

$$\phi(r')=2(I_0/c\sqrt{2\sigma\rho L})\Delta t\,\mathrm{jinc}^2(r'), \tag{13}$$

where r' is defined as r/L, the dimensionless distance. I_0 can be determined using Eq. (3), and by substituting into Eq. (13) we obtain the final form of the dimensionless initial potential:

$$\phi(r')=\pi\frac{V_p^2}{R}\eta\frac{\Delta t}{cL^{5/2}}\frac{1}{\sqrt{2\sigma\rho}}\mathrm{jinc}^2(r')=\phi_0\,\mathrm{jinc}^2(r'). \tag{14}$$

Transforming the equation of motion into dimensionless form by scaling with L and V, we obtain a set of equations that depend on the parameter

$$G=gL/V^2 \tag{15}$$

for the inviscid equations and the Reynold's number Re,

$$\mathrm{Re}=VL/\upsilon, \tag{16}$$

for the viscous problems with υ representing kinematic viscosity. For the case where $\lambda=0.5$ mm, $a=8$ mm, $z_0=48$ mm, and the liquid being water for which $\sigma=73$ mN/m, $\rho=1$ g/cm^3, and $\upsilon=1\times10^{-6}$ m^2/s, we obtain $F=3$, $L=3$ mm, and $V=22$ cm/s. The parameters of the problem, G and Re, are 0.6 and 660, respectively. These indicate that the gravity effects may be important in this problem, but the viscous effects (1/Re) are weak. On the other hand, if we use a transducer with an f number of 1, but still operate at the same frequency in water, $L=0.6$ mm and $V=0.5$ m/s will be obtained. In this case, $G=0.024$ and Re$=300$, resulting in both negligible gravitational and viscous effects.

B. Integral formulation

Here we consider an interface between a gas and a liquid, which is much more dense than the gas, so that the interface could be imagined to be composed of incompressible liquid and vacuum. The flow is assumed to be irrotational. With these assumptions, the flow can be expressed in terms of singular dipole solutions of Laplace's equation distributed over the deforming surface. The formulation is described in detail by Lundgren and Mansour.[11] Using Bernoulli's equation as the equation of motion, and Laplace's formula for the surface tension, the evolution equation can be expressed in terms of a velocity potential Φ. In Lagrangian coordinates, moving with the surface, we have

$$\frac{d\Phi}{dt}=-\frac{\sigma}{\rho}\nabla\cdot\mathbf{n}+gz+\frac{1}{2}\mathbf{u}\cdot\mathbf{u}, \tag{17}$$

where σ is the surface tension, $\mathbf{n}$ is the unit vector normal to the surface, g is the gravitational acceleration, z is the height of the surface with respect to a reference plane, and $\mathbf{u}$ is the velocity at the surface.

Given the potential at the surface, a dipole density μ may be determined from Φ by solving the integral equation

$$\Phi(\mathbf{r})=\frac{1}{2}\mu(\mathbf{r})+\mathrm{P.V.}\int_S\mu'\frac{\partial G(\mathbf{r},\mathbf{r}')}{\partial n'}dS', \tag{18}$$

where $G(\mathbf{r},\mathbf{r}')$ is the Green's function solution of Laplace's equation in an infinite domain, the principal value integration is over the surface S, and n is the direction normal to the surface. The integration is performed only at the interface or, in other words, at the surface. To compute the velocity of the surface, we introduce a vector potential $\mathbf{A}$ defined by the relation

$$\mathbf{A}=-\mathrm{P.V.}\int_S\mu'\mathbf{n}'\times\nabla_S G(\mathbf{r},\mathbf{r}')dS', \tag{19}$$

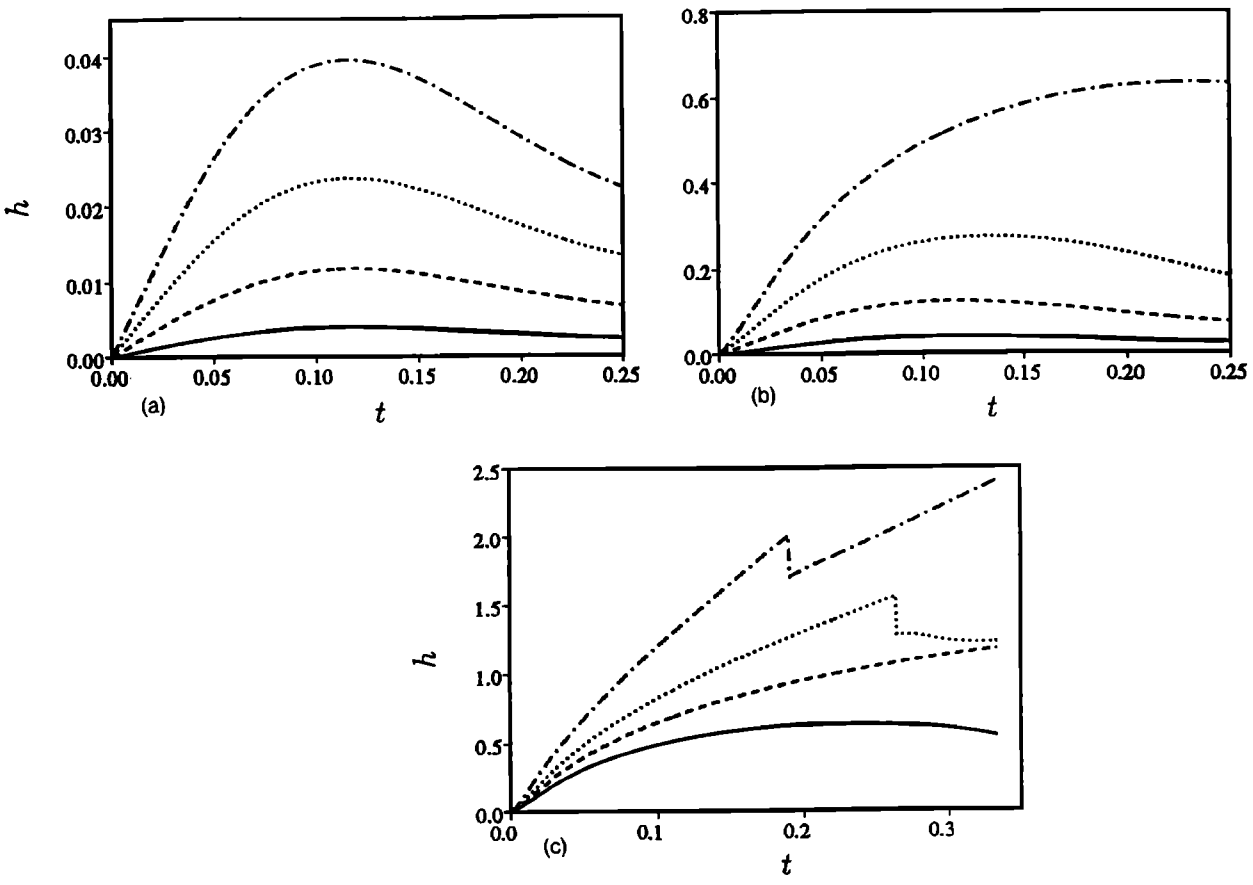

FIG. 3. Height of the mound at the origin for various ϕ_0. (a)– – – ϕ_0=0.01, - - - ϕ_0=0.03, · · · · · · · ϕ_0=0.06, - · - · - · ϕ_0=0.10; (b)– – – ϕ_0=0.10, - - - ϕ_0=0.30, · · · · · · · ϕ_0=0.60, - · - · - · ϕ_0=1.00; (c) – – – ϕ_0=1.00, - - - ϕ_0=1.25, · · · · · · · ϕ_0=1.50, - · - · - · ϕ_0=2.00.

where ∇_S is the gradient along the surface with respect to the integration variable $\mathbf{r}'$. We can then compute the normal and tangential components of the velocity of the surface by

$$\mathbf{u}\cdot\mathbf{n}=(\mathbf{n}\times\nabla)\cdot\mathbf{A}, \quad \mathbf{u}\cdot\mathbf{t}=\frac{\partial\Phi}{\partial s}. \tag{20}$$

The surface deforms according to the Lagrangian formula:

$$\frac{d\mathbf{r}}{dt}=\mathbf{u}. \tag{21}$$

The above equations (17)–(21) are solved by discretizing the surface into a set of node points. The positions of the nodes are tracked using the fourth-order Runge–Kutta approximation for advancement in time. All derivatives along the surface are computed using high-order Padé differencing, and the midpoint rule is used for spatial integration. The integral equation (18) is solved by iteration. The advantage of this method is that the numerical mesh is only on the free surface and can be concentrated enough to give an accurate representation of the surface. This is important because second derivatives of the surface

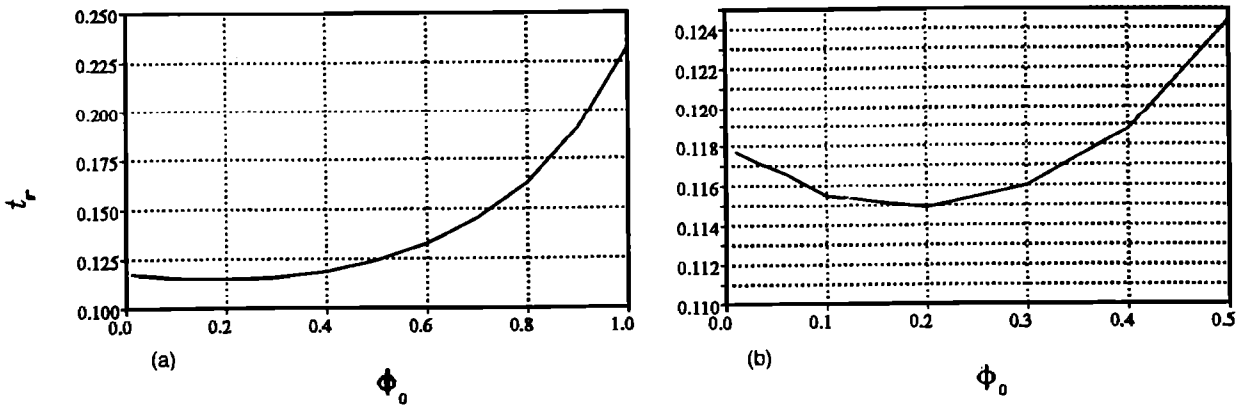

FIG. 4. (a) Time of mound formation t_f as a function of initial potential ϕ_0; (b) a close-up view.

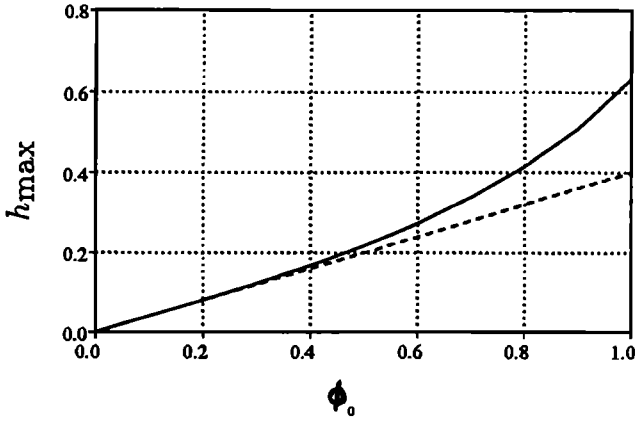

FIG. 5. Maximum height as a function of ϕ_0. ——— Computational results; --- curve fit $h_{max}=0.4\phi_0$.

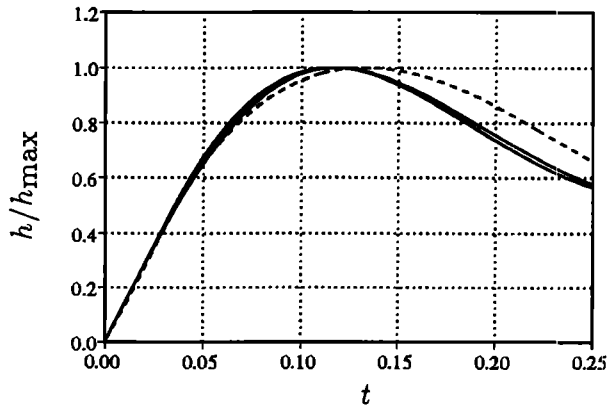

FIG. 6. Normalized height of mound as a function of time. – – – $0.01\leqslant\phi\leqslant0.3$; - - -$\phi=0.6$.

coordinates are needed in order to compute surface tension forces.

If we transform Eq. (17) into a dimensionless form by scaling with L and V [see Eqs. (10) and (11)], we get

$$\frac{d\Phi^*}{dt^*}=\frac{d\phi}{dt^*}=-\frac{1}{2}\nabla^*\cdot\mathbf{n}+Gz^*+\frac{1}{2}\mathbf{u}^*\cdot\mathbf{u}^*, \tag{22}$$

where * denotes the dimensionless quantities.

C. Results: Dimensionless

In this section, all the quantities used are dimensionless. In Fig. 3, we have plotted the height of the mound at $r'=0$ or, in other words, at the axis of symmetry for various initial ϕ_0. For ϕ_0 less than 1.5, the surface remains connected and we do not have drop ejection.[7] In this range, the surface rises and then collapses back. From Fig. 3, we find that the maximum height of the mound is proportional to ϕ_0, suggesting that the development of the mound is linear in ϕ_0. In this regime the nonlinear term $\mathbf{u}^*\cdot\mathbf{u}^*$ in Eq. (22) remains negligible. As we increase ϕ_0, the response becomes nonlinear.

In Fig. 4, we show the time of mound formation t_r as a function of ϕ_0. The most interesting finding is that, in the linear regime, the time when the mound reaches its maximum height seems to be independent of ϕ_0. Figure 4(b) shows that there is less than 2% variation in t_r for a factor of 40 variation in ϕ_0. The most important implication of this finding is that the input power in the linear range is not an important factor in determining the time of mound formation. This is due to the fact that the surface acts like a membrane with a characteristic length and a characteristic velocity ($V=\sqrt{2\sigma/\rho L}$). Therefore, we have a characteristic frequency V/L, which is the inverse rise time.

Figure 5 shows the maximum height h_{max} as a function of ϕ_0. We have also plotted, on the figure, the curve $h=0.4\phi_0$ as an approximation to the development of maximum height as a function of ϕ. We find that, in fact, for small ϕ_0 (<0.4), the maximum height is linearly proportional to ϕ_0. This observation, combined with the fact that t_r is independent of ϕ_0, implies that the curves in Fig. 3(a), and the first two curves in Fig. 3(b), will collapse under normalization with h_{max}. Figure 6 demonstrates this result.

We conclude that, if gravity effects are negligible, the curve that best fits the curves shown as solid lines in Fig. 6 is the characteristic response curve of the liquid surface for a low-amplitude jinc$^2(\cdot)$ impulse. This response curve is valid for all lenses, for all surface tensions, and for all input powers, as long as they remain in their proper ranges. This is the most important result of this analysis, and the predictions from this response curve are in very good agreement with the experimental results.

D. Results: Dimensional

As seen in Fig. 4, t_r is approximately 0.116. This is the dimensionless time of mound formation. In order to convert t_r to dimensional figures, we multiply by the time scale T, given in Eq. (12). This yields

$$t_{\text{dimensional}}=0.116\,\frac{2\lambda^{3/2}F^{3/2}\rho^{1/2}}{\sigma^{1/2}} \tag{23}$$

or, when solved for surface tension,

$$\sigma=0.0538\,\frac{\lambda^3F^3\rho}{(t_{\text{dimensional}})^2}. \tag{24}$$

For water with $\sigma=73$ mN/m, $\rho=1000$ kg/m^3, the theoretical values in Table I are obtained. In Sec. III, we present the experimental results and compare them with the computed results shown in Table I.

TABLE I. Experimentally observed rise time compared with theoretical calculation for clean water.

Case	Frequency (MHz)	F number	Experimental $t_{\text{dimensional}}$ (μs)	Theoretical $t_{\text{dimensional}}$ (μs)	Percentage difference
1	3.0	3	1270	1577	19.6
2	3.0	1	312	304	−2.6
3	10.0	3	263	259	−1.5

III. THE EXPERIMENTAL SYSTEM AND RESULTS

The purpose of these experiments is to determine the dependence of rise time on surface tension and incident acoustic energy. A confocal optical microscope[12] tracks the variations of the water surface displacement caused by the radiation pressure associated with the acoustic pulse. The laser beam from the confocal microscope is carefully positioned, as shown in Fig. 1, over the center of the water mound by maintaining circularly symmetric refraction of the beam by the mound surface. The signal corresponding to the depth variations of the surface is digitized at 100 kilosamples per second conversion rate with 12 bits resolution. The depth response $V(z)$ of the confocal microscope[13] is measured before each data acquisition to

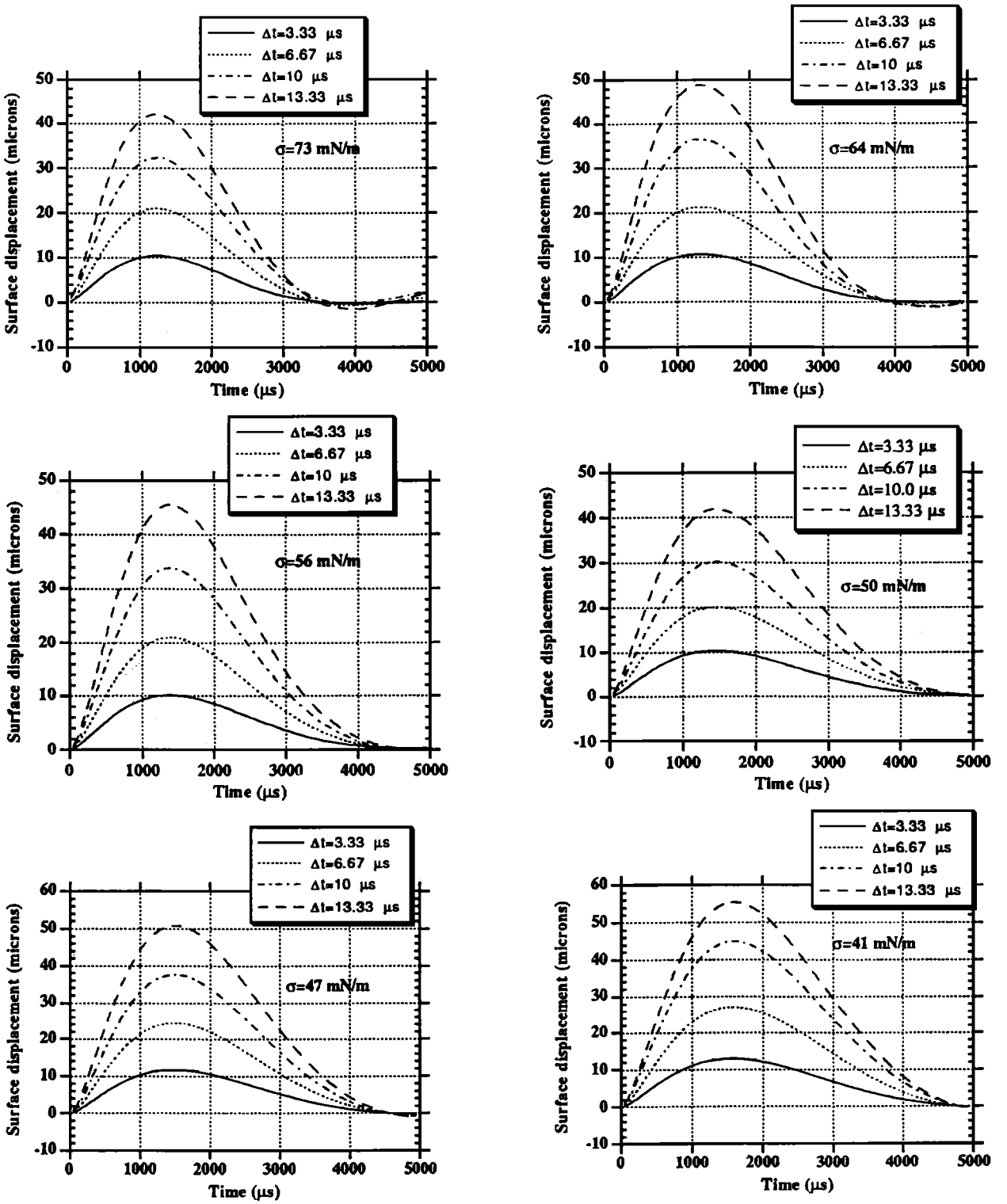

FIG. 7. Experimentally measured rise time as a function of surface tension for various pulse amplitudes and pulse widths. Frequency of operation is 3 MHz and f number is 3.

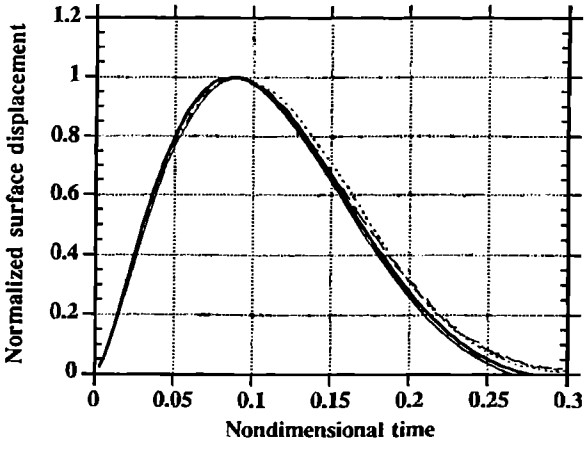

FIG. 8. Normalized surface displacement versus dimensionless time for V_p=6.7 V, Δt=3.33 μs at 3 MHz. Individual plots are for different surface tension values.

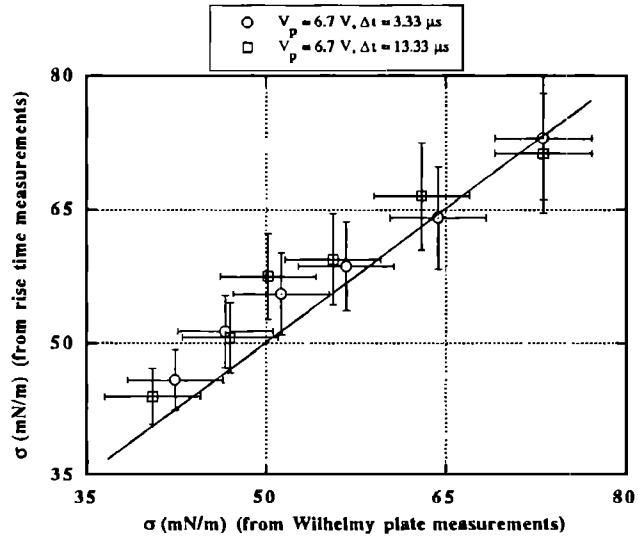

FIG. 9. Comparison of the two techniques of surface tension measurements. Vertical axis values are obtained by the rise-time measurements and horizontal axis values are measured by the Wilhelmy plate technique.

minimize the effects of mechanical and electronic drifts. The $V(z)$ measurements are performed by raising the water level at a constant rate and acquiring the signal from the microscope as a function of time. Then, the time axis of each $V(z)$ data is converted into distance z. Knowing the depth response, we transform the voltage signals from the microscope during the measurements into true displacement data. Even for large signal swings, this transformation compensates for the nonlinearities of $V(z)$. The water surface is always kept at the focal plane of the ultrasonic transducer by maintaining the time delay of the first acoustic echo constant.

We varied the incident acoustic pulse energy in two ways: by varying the amplitude V_p or by varying the pulse width Δt. We also altered the surface tension by adding minute amounts of the surfactant sodium dodecyl sulfate (SDS) into water. Thus, we were able to lower the surface tension σ from 73 mN/m, the value for clean water at 20 °C, down to 40 mN/m. The surface tension measurements were done by the Wilhelmy plate technique.[14] The excitation amplitude V_p was always maintained at 6.7 V, while the pulse width was increased in four equal steps. According to the velocity potential analysis, for ϕ_0 less than 0.4, operation is in the linear regime, as indicated in Fig. 5. The choice of V_p=6.7 V and Δt=13.33 μs for clean water causes ϕ_0 to be 0.00037, which is much less than 0.4. This result is clearly reflected in the experimental data, as shown in Fig. 7. As seen from the figure, for the same surface tension, as the incident pulse energy increases (increasing the pulse width), the displacement varies almost linearly. The rise-time calculations are performed by curve fitting to experimental surface displacement data and finding the time t_r where the maximum displacement occurs. The rise time t_r also remains constant with a given surface tension as the incident acoustic energy increases. For clean water, a comparison between the experimental and theoretical rise times is shown in Table I.

In Fig. 8, we have normalized the surface displacements for V_p=6.7 V and Δt=3.33 μs at different surface tensions, and we have nondimensionalized the time axis for each piece of data, according to Eq. (12). As discussed earlier, under this transformation all the individual plots should collapse into a single plot. Figure 8 provides experimental proof for this theoretical prediction.

There are two major error sources in the experimental system. The first one is in the time resolution of the data. The analog-to-digital conversion process introduces ±10 μs uncertainty in time resolution of the raw data. The second source of error is the ambient capillary waves in the measurement tank that are induced by the airflow in the room. Since the acoustically generated displacement of the water surface is on the order of 10 μm, those vibrations can contribute significantly to the detected signal. This problem can be remedied by acquiring data under the same conditions many times and averaging afterward. We did not apply this technique because of drifts in the optical setup. Under the worst conditions, the error in measurements of the time of mound formation is less than ±30 μs by observation of the scatter of the data obtained from the repetitive measurements in clean water. We can claim ±2 mN/m accuracy in Wilhelmy plate measurements. In Fig. 9, we plotted the surface tension values calculated from Eq. (24) against the Wilhelmy plate measurements with their respective error bars for two different acoustic excitations where V_p=6.7 V and Δt=3.33 and 13.33 μs. In using Eq. (24) for surface tension, we took the time of mound formation for clean water for excitation conditions of V_p=6.7 V and Δt=13.33 μs as the reference. The solid line in Fig. 9 represents the ideal case where the measurements from two techniques are identical. As seen from the figure, the ideal line intersects the data points when the error bars are taken into account.

IV. DISCUSSION AND CONCLUSIONS

We also experimentally investigated the effect of increasing the incident acoustic pulse amplitude on the rise time. The rise time seems to decrease with increasing pulse amplitude, even though the pulse energies are still much lower than the theoretically predicted linearity limit. This unexpected result may be due to nonlinear propagation in water. A sinusoidal waveform will be distorted to an ideal sawtooth waveform because of nonlinear propagation through a distance called discontinuity distance, as discussed by Beyer.[15] For our experimental configuration, we found the depth of focus of the particular transducer is comparable to the discontinuity distance. Based on this argument, a qualitative explanation can be proposed: Generation of higher harmonics by transformation into a sawtooth waveform will cause the effective wavelength at the focal spot to decrease. As seen from Eq. (23), decreasing the wavelength λ will decrease the rise time $t_{\text{dimensional}}$, which is in accordance with our experimental observations.

This technique stands out as a very promising method of measuring surface tension, especially when surfactants are present on the liquid. The measurement is relatively fast because typical rise times are of the order of milliseconds. Averaging techniques can successfully be applied to increase the accuracy of the measurement by acquiring several thousand data sets in a few seconds. The technique is also insensitive to reasonable variations or drifts in electronics. Most importantly, it is independent of the amplitude of the acoustic excitation, as long as it is kept below a certain threshold, which is a function of transducer and liquid characteristics. Lastly, it has a distinct advantage over many other techniques by being a noncontacting method.

ACKNOWLEDGMENTS

This work was made possible by support from the Office of Naval Research under Contract no. N00014-86-K-0433. We also would like to thank the reviewer for valuable comments.

[1] Lord Rayleigh, Philos. Mag. **3**, 338–346 (1902).
[2] Lord Rayleigh, Philos. Mag. **10**, 364–374 (1905).
[3] R. T. Beyer, "Radiation pressure—the history of a mislabeled tensor," J. Acoust. Soc. Am. **63**, 1025–1030 (1978).
[4] J. A. Rooney and W. L. Nyborg, "Acoustic radiation pressure in a traveling plane wave," Am. J. Phys. **40**, 1825–1830 (1972).
[5] B. T. Chu and R. E. Apfel, "Acoustic radiation pressure produced by a beam of sound," J. Acoust. Soc. Am. **72**, 1673–1687 (1982).
[6] J. A. Rooney, "Nonlinear phenomena," in *Methods of Experimental Physics* (Academic, New York, 1981), Vol. 19.
[7] S. A. Elrod, B. Hadimioglu, B. T. Khuri-Yakub, E. G. Rawson, E. Richley, C. F. Quate, N. N. Mansour, and T. S. Lundgren, "Nozzleless droplet formation with focused acoustic beams," J. Appl. Phys. **65**, 3441–3447 (1989).
[8] C. Cinbis and B. T. Khuri-Yakub, "Noncontacting measurement of surface tension of liquids," Rev. Sci. Instrum. **63**, 2048–2050 (1992).
[9] G. S. Kino, *Acoustic Waves: Devices, Imaging and Analog Signal Processing* (Prentice-Hall, Englewood Cliffs, NJ, 1987).
[10] N. N. Mansour and T. S. Lundgren, "Satellite formation in capillary jet breakup," Phys. Fluids A **2**, 1141–1144 (1990).
[11] T. S. Lundgren and N. N. Mansour, "Oscillations of drops in zero gravity with weak viscous effects," J. Fluid Mech. **194**, 479–510 (1988).
[12] G. Q. Xiao, T. R. Corle, and G. S. Kino, "Real-time confocal scanning optical microscope," Appl. Phys. Lett. **53**, 716–718 (1988).
[13] T. R. Corle, C-H. Chou, and G. S. Kino, "Depth response of confocal optical microscopes," Opt. Lett. **11**, 770–772 (1986).
[14] C. Cinbis, "Noncontacting techniques for measuring surface tension of liquids," Ph.D. dissertation, Stanford University, Stanford, California (1992).
[15] R. T. Beyer, *Nonlinear Acoustics*, Naval Ship Systems Command, #O-596-215 (U.S. Government Printing Office, Washington, DC, 1974), pp. 101–105.